Dendritic growth patterns in rocks: Inverting the driving and triggering mechanisms

Chong Liu[1,2], Victor M. Calo[3], Klaus Regenauer-Lieb[2,4], Manman Hu[1]

[1]Department of Civil Engineering, The University of Hong Kong, Hong Kong, China
[2]WA School of Mines: Minerals, Energy and Chemical Engineering, Curtin, Bentley, WA 6102, Australia
[3]School of Electrical Engineering, Computing and Mathematical Sciences, Curtin University, P.O. Box U1987, Perth, WA 6845, Australia
[4]School of Minerals and Energy Resources Engineering, UNSW, Sydney, NSW 2052, Australia

Key Points:

- Introduction of a general classification criterion for dendritic morphologies;
- Fractal dendritic morphology diagram reproduces natural dendrite patterns;
- Compared to Liesegang patterns, dendrites require higher fluid diffusivity and tend to grow along interfaces;
- Inversion of phase-field diffusivity and self-diffusion coefficient of solute is possible from photographic images of dendritic patterns.

Corresponding author: Manman Hu, mmhu@hku.hk

Abstract
Mineral precipitation can form complex patterns under non-equilibrium conditions, in which two representative patterns are rhythmic Liesegang stripes and fractal dendrites. Interestingly, both patterns occur in the same rock formations, including various dendritic morphologies found in different rocks, such as limestone and sandstone. However, the underlying mechanism for selecting the vastly different mineral precipitation patterns remains unclear. We use a phase-field model to reveal the mechanisms driving pattern selection in mineral precipitation. Simulations allow us to explore the effects of diffusion parameters on determining the dendritic morphologies. We also propose a general criterion to distinguish the resulting dendrites in simulations and field observations based on a qualitative visual distinction into three categories and a quantitative fractal dimension phase diagram. Using this model, we reproduce the classified dendrites in the field and invert for the key parameters that reflect the intrinsic material properties and geological environments. This study provides a quantitative tool for identifying the morphology selection mechanism with potential applications to geological field studies, exploration for resource evaluation, and other potential industrial applications.

Plain Language Summary

Dendrites are branched, tree-like structures that are found in various natural and biological systems. In the context of mineral precipitation or crystal growth, dendrites refer to the branching patterns formed by the deposition of minerals or crystals in a non-equilibrium environment. Other patterns frequently found in these reactive systems are concentric ring-like or striped patterns called Liesegang patterns. Although these patterns occur in the same rock formations, the mechanism for selecting different mineral precipitation patterns is not well understood. Here we use a phase-field model to explore how different diffusion parameters affect the selection of dendritic morphologies. We propose a criterion to distinguish different dendrites in simulations and field observations based on a qualitative visual distinction (needle-like, tree-like and seaweed-like) and a quantitative fractal dimension phase diagram. The model can be deployed to invert for the intrinsic rock properties as well as the geological environments these dendrites grow in. The numerical scheme is robust and efficient, allowing easy implementation of add-on features in the future for potential applications across scientific and engineering disciplines.

1 Introduction

A wide variety of patterns appear in nature. Their formation mechanism has been a special focus of interest for the early philosophers, artists and the scientific community. Examples are many and varied, ranging from spiral waves in the Belousov–Zhabotinsky redox reaction (Yamaguchi et al., 1991) to disordered-branching patterns in electrochemical deposition systems (Arguello et al., 2022), from the formation of Liesegang stripes (Liesegang, 1906; Liu et al., 2023a) to dendritic growth in reaction-diffusion systems (Chopard et al., 1991; Z. Xu & Meakin, 2008), from oil recovery by fluid injection (Furui et al., 2022) to mineral precipitation during geologic sequestration (T. Xu et al., 2003). Understanding the underlying physical mechanism of pattern-forming processes is of significant interest in science and technology. In the present work, we focus on mineral precipitation observed in many rock textures in geology by reactive transport processes (Ladd & Szymczak, 2021; Molins et al., 2021)‘, particularly reaction-diffusion processes without considering the advective effect (Steefel & Maher, 2009). Mineral precipitation reactions have been argued to form as a result of the following: (i) self-organized processes involving coupled mass transport and precipitation, as in the case of Liesegang structures; (ii) intrinsic instabilities during the growth of the crystal, as in the case of Mullins–Sekerka instability (Mullins & Sekerka, 1963) leading to dendritic patterns (García-Ruiz & Otálora,

2015). Interestingly, both patterns are observed in the same rock, either as a pervasive structure through the entire rock (Liesegang stripes) or on sedimentary surfaces (dendritic growth), as shown in Figure 1 collected from the Solnhofen limestone, Bavaria state of Germany. In Liesegang stripes, a moving reaction-diffusion front propagates from the

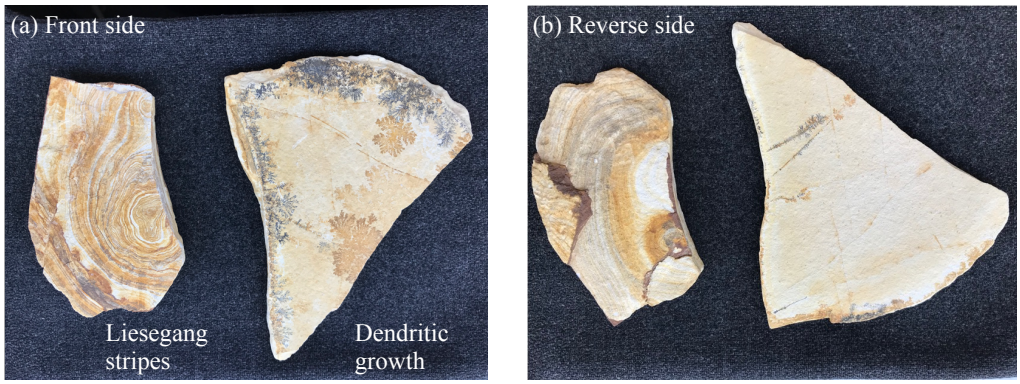

Figure 1. Two distinct patterns in Solnhofen limestone: Liesegang stripes and dendritic growth. (a) Front and (b) reverse sides illustrate that Liesegang rings penetrate through the sedimentary layers while dendrites nucleate along discontinuities in the sedimentary bedding layers, such as cracks and joints and their growth is restricted to sedimentary layers.

center to the far field forming rhythmic patterns. In contrast, dendritic growth emerges as a competition between the mineral concentration diffusion and interfacial effects, such as anisotropy, surface tension and kinetics (Langer, 1989).

The dendritic structure and growth mechanism in Solnhofen limestone have been attributed to a reaction-diffusion mechanism (Chopard et al., 1991). The authors also proposed that the approach could explain the formation of 'Liesegang bands' in the same rock. However, they note that some features of these bands are not captured by their model; in particular, the temporal and length scales are inappropriate. Herein, we seek to find the cause for the nucleation of precipitation patterns by vastly different time-scale of the multifaceted morphogenic processes.

The Liesegang phenomenon has gained much attention after being discovered at the end of the nineteen century (Liesegang, 1906). Several celebrated theoretical models have sought to describe the mechanism underlying the Liesegang phenomenon, like the supersaturation model (Ostwald, 1902), the sol-coagulation model (Büki et al., 1995), and phase separation theory (Antal et al., 1998; Thomas et al., 2013). Two main features of the Liesegang patterns are studied in the literature. First, the profound characteristic is the striking periodic stripes following simple empirical laws, particularly time, spacing, width, and Matalon-Packter laws (Matalon & Packter, 1955; Chopard et al., 1994; Antal et al., 1999). Second, the dynamic transition of rhythmic bands towards more complex and irregular exists, like spotted patterns or combined stripes and spots, such as Mississippi Valley Type deposits (Wang et al., 2015). For more detailed information, see our recent work that decoded important coefficients governing the time scales of the formation of Liesegang patterns in rocks from a thermodynamic perspective (Liu et al., 2023a).

We propose to fill this research gap by posing the following three essential questions to the pattern selection mechanism: (i) what causes the regime variation from Liesegang stripes to dendritic growth; (ii) is it possible to establish a general criterion to distinguish dendrite emergence through the qualitative description and quantitative analysis; (iii) how a computational model can reproduce the wide range of dendritic morpholo-

gies observed on rock surfaces. To unveil the mechanism behind the two distinct patterns and varying morphologies of dendrites, we rely here on a numerical model for conducting a comprehensive investigation over the overall appearance of structures.

Dendritic growth leads to the dynamic evolution of the solid-liquid interfaces during reactive transport processing, particularly mineral precipitation, so a key problem is to track the corresponding moving boundary. To this end, different interface tracking techniques have been developed to capture the mineral-fluid interfaces during the past several decades, such as particle-based and grid-based approaches. The particle-based methods are less popular to the grid-based methods due to high computational costs and statistical noise (Ladd & Szymczak, 2021), for instance, Lattice Boltzmann method (Kang et al., 2003) and smoothed-particle hydrodynamics (Tartakovsky et al., 2007). The grid-based approaches capture the interface in both sharp-interface and smear-interface manners. The sharp-interface methods track interfaces explicitly for the associated boundary conditions and capture the basic underlying physics with associated length and time scales, but they suffer difficulties for higher-dimensional practical problems with dynamic topology evolution, e.g. fragmentation and coalescence occurring, such as Level-set methods (Li et al., 2008). The diffuse-interface approximation avoids the tracking by implicitly resolving interfaces for specific boundary conditions through the solution scheme. The standard diffuse-interface approach is called the volume of solid approach that relies on porosity to implicitly track the solid-liquid boundary with the fine meshes, but it needs to enforce mass conservation at the interface (Steefel & Lasaga, 1994; Soulaine & Tchelepi, 2016). To address this problem, we choose an alternative diffuse-interface method, called the phase-field method, to simulate dendritic growth, where the interface boundary condition can be satisfied without adding an additional mass balance equation at some vertices of the solid-liquid interfaces. This makes the phase-field method a more efficient and versatile tool to study interface-related problems, such as phase separation, multiphase flows, fracture propagation, and microstructure evolution (Langer, 1980; Gómez et al., 2008; DeWitt et al., 2020; Fei et al., 2022; Behnoudfar et al., 2022; Espath, 2021; Espath & Calo, 2021). Phase-field simulations use an order parameter to represent each phase in the system, such as the solid and liquid phases denoted by the magnitude of the order parameter (e.g., 1 and -1, respectively), while the continuous variation from -1 to 1 represents the solid-liquid interface. Compared to the sharp-interface approaches, the method requires sufficiently fine meshes across the interface to capture its dynamic evolution ensuring numerical accuracy. Therefore, the phase-field method is here employed to analyze the evolution of the dendrite growth versus the Liesegang pattern formation. The simulation is accelerated using a locally adaptive mesh refinement method at the interface while retaining a coarse mesh in the rest of the domain (Rosam et al., 2007; Hu et al., 2009; DeWitt et al., 2020; Giraldo & Calo, 2023; Cier et al., 2021).

The phase-field method was first attempted by Ivantsov (1947) to describe the growth of the dendritic tip analytically and showed a rotational paraboloid, excluding the capillary and kinetic effects. Simplified phase-field models were then adopted to describe the formation of dendritic morphologies in the pure-substance solidification of various materials (Collins & Levine, 1985; Caginalp, 1986, 1989; Kobayashi, 1993). Among them, Brener et al. (1996) proposed a morphological diagram to distinguish simulated dendritic patterns in the supercooling and anisotropy space. The diagram separates them into four categories based on two qualitative identifiers: (i) seaweed as opposed to dendrites as the basic patterns and (ii) fractal contrary to compact patterns. Later, Karma and Rappel (1998) took capillary and kinetic effects into account and found that a small perturbation can trigger a dramatic change in morphologies of both 2-D and 3-D simulations. Although most of the early studies focussed on thermally-induced dendritic solidification from a supercooled liquid, the concentration-driven dendrites, in our case of mineral precipitation patterns, share similar features as stated by Langer (1980); this similarity enables us to use a generic deposition model to capture the solid-liquid interface evolution due to mineral precipitation. During solidification, two common assumptions

exist for the concentration field across the solid-liquid interface. Z. Xu and Meakin (2008, 2011) assumed a discontinuous solute concentration field between the solid and liquid phases. They derived a governing formulation for dissolution-precipitation processes and demonstrated that it reproduces fingering patterns and diffusion-limited precipitation based on Kappa's model (Karma & Rappel, 1998). The discontinuous model was advanced to include advection effects for transitional flows when applied to pipe precipitation (Hawkins et al., 2014) and the dissolution wormhole formation during oil and gas recovery (Furui et al., 2022). Although the updated model gives a good estimate of the fractal dimension observed in diffusion-limited aggregation or dissolution, the formed patterns differ from a phenomenological viewpoint. In contrast, Karma and Rappel (1998) used a continuous variable through the interfaces, an assumption extensively adopted for alloy precipitation and electrochemical precipitation and generates a rich variety of dendrites (Brener et al., 1996; Vignal et al., 2017).

To address the earlier questions, here we utilize the model of (Karma & Rappel, 1998) to simulate the pattern formation of mineral precipitation. We first adopt an effective criterion to classify the observed dendrites qualitatively. We then perform 2-D simulations to explore the influences of three control parameters on the dendritic morphology selection. Using this criterion, we establish a systematic morphological diagram for those parameters and classify the resulting patterns using the phenomenological classification criterion. Finally, we propose a quantitative phase diagram to distinguish dendritic morphologies in each category by measuring their fractal dimensions.

The rest of this study is organized as follows. In Section 2, we present the phase-field method adopted for modelling mineral precipitation. The method of fractal dimension calculation and its implementation are described. In Section 3, we present a convergence study and comprehensive investigation on the variety of dendritic growth. The numerical simulation results are compared with the observations from natural samples of dendritic patterns. Section 4 discusses the difference between Liesegang stripes and dendritic growth and proposes its implication for pattern selection mechanisms in industrial applications, mainly in mineral and thermal energy storage fields. Finally, we conclude our study in Section 5.

2 Methodology

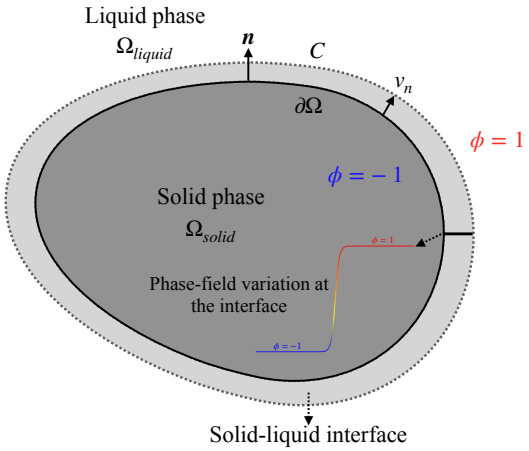

Figure 2. Sketch illustrating the solute precipitation

We study the evolution of the solid-liquid interface during solute precipitation processes considering a 2-Dimensional domain, as illustrated in Figure 2. The growing solid-

liquid interface is denoted as $\partial\Omega$ separating the solid phase and the fluid phase, denoted as Ω_{solid} and Ω_{liquid}, respectively. We assume that the dendritic patterns observed on rock surfaces in Figure 1 are formed by mineral precipitation due to chemical reactions enabled by mass flux driven by a concentration gradient. Advective flux is considered negligible.

2.1 Mineral precipitation model

The solute precipitation mathematical model contains a liquid phase diffusion process and a first-order reaction at the solid-liquid interface. Diffusive processes in the solid phase are ignored. The solute diffusion in the liquid phase follows Fick's law

$$\frac{\partial C}{\partial t} = D\Delta C, \quad \text{in } \Omega_{liquid}, \tag{1}$$

where C is the solute concentration, which varies in space and time. D denotes the solute diffusivity coefficient.

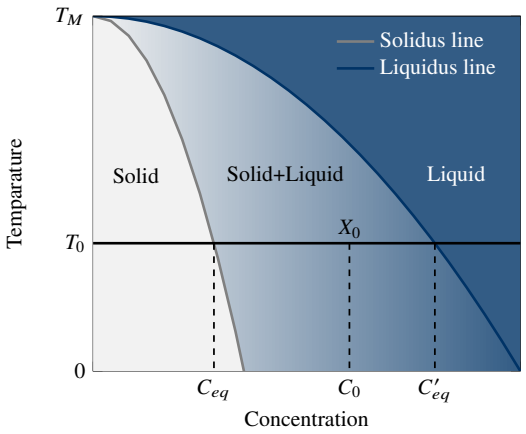

Figure 3. Portion of the phase diagram of a binary solution

At the solid-liquid interface, the mass balance prescribes the relationship between the solute flux onto the solid phase and the reactive precipitation rate

$$D\nabla C \cdot \boldsymbol{n} = k(C - C_{eq}), \quad \text{on } \partial\Omega, \tag{2}$$

where $\boldsymbol{n}$ is the unit normal vector of the solid-liquid interface pointing towards the liquid phase Ω_{liquid} as illustrated in Figure 2. C_{eq} is the equilibrium solute concentration in the solid. The initial solute concentration C_0 is assumed under the local temperature T_0, a constant in the whole domain. Considering isothermal precipitation, the solid-liquid interface grows when the solute concentration in the liquid C'_{eq} is greater than that in the solid C_{eq} in the two-phase equilibrium. The growth rate of the precipitate is proportional to the reaction rate as

$$\rho_s v_n = k_c k(C - C_{eq}), \quad \text{on } \partial\Omega, \tag{3}$$

where ρ_s is the solid density, v_n is the precipitation growth rate in the normal direction. k_c and k are the reaction rate and stoichiometric coefficients of order unity.

Equation (3) states a local mass conservation condition at the interface that propagates because of solute precipitation. In addition, the curvature of the interface may

affect the equilibrium concentration through the surface tension effect (known as the Gibbs-Thomson effect), thereby altering the normal growth velocity (Karma & Rappel, 1998). By normalizing the solute concentration by the equilibrium concentration as

$$c = \frac{C - C_{eq}}{C_{eq}}$$

we rewrite (1)-(3) as

$$\frac{\partial c}{\partial t} = D\Delta c, \qquad \text{in } \Omega_{liquid}, \tag{4}$$

$$v_n = D\nabla c \cdot \boldsymbol{n}, \qquad \text{on } \partial\Omega, \tag{5}$$

$$c = \beta v_n - d_0(\theta)\kappa, \qquad \text{on } \partial\Omega, \tag{6}$$

where $d_0(\theta)$ and κ are the anisotropic capillary length and interface curvature, respectively; β is the interface kinetic coefficient relevant to the reaction rate. Here, we define the solute concentration $c = -\Psi$ far from the solid-liquid interface, where

$$\Psi = \frac{C_{eq} - C_\infty}{C_{eq}},$$

which denotes the dimensionless supersaturating and C_∞ the initial solute concentration of the supersaturated liquid. The supersaturation value Ψ is usually normalized to a maximum value of 1 (Karma & Rappel, 1998; Singer et al., 2006; Gómez et al., 2008).

2.2 Phase-field model for mineral precipitation

The direct solution of the sharp-interface model (4)–(6) requires tracking the spatial-temporal evolution of the free boundary. Alternatively, herein, we employ the phase-field model proposed by Karma and Rappel (1998) to solve dendritic growth numerically due to solute precipitation. The dissipation of the free energy derives from phase-field models. The free energy potential F for dendritic growth can be written as

$$F(\phi, \nabla\phi, c) = \int_\Omega f(\phi, \nabla\phi, c) dV_\Omega \tag{7}$$

where c is the solute concentration and ϕ represents the phase-field variable (i.e., the order parameter). The order parameter ϕ takes values in the range of $[-1, 1]$, where the convention $\phi = -1$ and $\phi = 1$ indicate the solid and liquid phases, respectively, and the diffusion interface is between $(-1, 1)$. The phase-field variable is a non-conserved order parameter tracking the progress of the precipitation process. f is the free energy density consisting of two contributions

$$f(\phi, \nabla\phi, c) = I_\phi + B_\phi \tag{8}$$

where I_ϕ is the contribution from the interface energy and B_ϕ is the free energy of the bulk. The interface energy localizes to the interface with a simple expression

$$I_\phi = \frac{1}{2} W(\boldsymbol{n})^2 |\nabla\phi|^2 \tag{9}$$

where $W(\boldsymbol{n})$ is the gradient energy coefficient closely associated with the thickness of the interface. In 2D, we express $W(\boldsymbol{n}) = W_0 a(\boldsymbol{n})$, a simple form including in-plane symmetry gives

$$a(\boldsymbol{n}) = 1 + \varepsilon_m [m \cos(\theta - \theta_0)] \tag{10}$$

where m is a non-negative integer reflecting the number of the main branches of one dendrite, θ is the in-plane azimuthal angle denoted by $\tan(\theta) = n_y/n_x$, θ_0 is the initial offset azimuthal angle, and ε_m denotes the strength of the anisotropy.

The second right-hand-side term B_ϕ in (8) models the bulk energy phase, a double-well potential with two minima corresponding to the solid and liquid phases. The simple polynomial formulation couples the solute concentration c with the phase-field variable ϕ to model the concentration's effect on the bulk free energy density

$$B_\phi = -\frac{1}{2}\phi^2 + \frac{1}{4}\phi^4 + \lambda c\phi\left[1 - \frac{2}{3}\phi^2 + \frac{1}{5}\phi^4\right] \tag{11}$$

where λ is a dimensionless coupling parameter. We satisfy the solvability condition (Karma & Rappel, 1998; Singer et al., 2006; Gómez et al., 2008) by making λ take the following form

$$\lambda = \frac{D\tau_0}{0.6267W_0^2} \tag{12}$$

where τ_0 is the relaxation time coefficient. This λ selection allows us to model the sharp interface of dendritic growth as the "diffuse-interface" limit.

The evolution equations for the phase-field variable are given by either the Cahn-Hilliard or the Allen-Cahn equation, depending on whether the field is conserved. The phase-field variable, non-conserved quantity, evolves by the Allen-Cahn equation, which indicates the variational derivative of the free energy potential with respect to the phase-field variable ϕ gives the force promoting the temporal evolution of the field ϕ

$$\tau(\boldsymbol{n})\frac{\partial\phi}{\partial t} = -\frac{\delta F}{\delta\phi}, \tag{13}$$

where $\tau(\boldsymbol{n})$ is the kinetic coefficient taking a form $\tau(\boldsymbol{n}) = \tau_0 a(\boldsymbol{n})$. The detailed variational derivative in (13) in 2D is

$$\begin{aligned}\tau(\boldsymbol{n})\frac{\partial\phi}{\partial t} =& [\phi - \lambda c(1-\phi^2)](1-\phi^2) + \nabla\cdot\left([W(\boldsymbol{n})]^2\nabla\phi\right) \\ &+ \frac{\partial}{\partial x}\left[|\nabla\phi|^2 W(\boldsymbol{n})\frac{\partial W(\boldsymbol{n})}{\partial\left(\frac{\partial\phi}{\partial x}\right)}\right] + \frac{\partial}{\partial y}\left[|\nabla\phi|^2 W(\boldsymbol{n})\frac{\partial W(\boldsymbol{n})}{\partial\left(\frac{\partial\phi}{\partial y}\right)}\right],\end{aligned} \tag{14}$$

The reaction-diffusion equation considering mineral precipitation or dissolution governs the temporal evolution of the solute concentration at the interface such that

$$\frac{\partial c}{\partial t} = D\nabla^2 c + A\frac{\partial\phi}{\partial t}. \tag{15}$$

The last term in (15) is a solute source or sink, indicating the consumption or production of ions by the porous mineral (Ladd & Szymczak, 2021). This term is localized near the interface, while it is neglected outside of the diffusive interface region. As the phase field variable ϕ takes range in [-1,1], it follows that $A = \rho_s/2C_{eq}k_c = 1/2$ in the sharp interface limit (Z. Xu & Meakin, 2008).

We introduce an intermediate variable μ (a.k.a. chemical potential or driving force)

$$\begin{aligned}\mu =& [\phi - \lambda c(1-\phi^2)](1-\phi^2) + \nabla\cdot\left([W(\boldsymbol{n})]^2\nabla\phi\right) \\ &+ \frac{\partial}{\partial x}\left[|\nabla\phi|^2 W(\boldsymbol{n})\frac{\partial W(\boldsymbol{n})}{\partial\left(\frac{\partial\phi}{\partial x}\right)}\right] + \frac{\partial}{\partial y}\left[|\nabla\phi|^2 W(\boldsymbol{n})\frac{\partial W(\boldsymbol{n})}{\partial\left(\frac{\partial\phi}{\partial y}\right)}\right],\end{aligned} \tag{16}$$

making the governing equations more compact. Thus, rearranging (14) and (15), we get

$$\tau(\boldsymbol{n})\frac{\partial\phi}{\partial t} = \mu, \tag{17}$$

$$\frac{\partial c}{\partial t} = D\nabla^2 c + A\frac{\mu}{\tau(\boldsymbol{n})}, \tag{18}$$

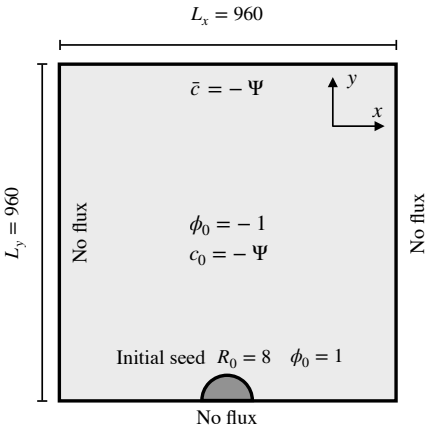

Figure 4. Sketch of initial & boundary conditions for dendritic growth

2.3 Definition of the numerical problem

Considering an initial–boundary value problem in a square domain, as shown in Figure 4, we denote the domain as $\Omega \in \mathbb{R}^2$ and its external boundary as Γ which has a unit outward normal vector $\boldsymbol{n}$. We impose essential and natural boundary conditions for the solute concentration c, the phase-field variable ϕ, and the driving force μ. Let Γ_a, Γ_b and Γ_c denote the essential boundaries for the concentration and phase field, respectively, and Γ_d, Γ_e and Γ_f are the natural boundaries. These boundaries satisfy

$$\overline{\Gamma_a \cap \Gamma_d} = \overline{\Gamma_b \cap \Gamma_e} = \overline{\Gamma_c \cap \Gamma_f} = \emptyset \tag{19}$$

$$\overline{\Gamma_a \cup \Gamma_d} = \overline{\Gamma_b \cup \Gamma_e} = \overline{\Gamma_c \cup \Gamma_f} = \Gamma \tag{20}$$

The essential boundary conditions read

$$c = \bar{c} \quad \text{on } \Gamma_a; \qquad \phi = \bar{\phi} \quad \text{on } \Gamma_b; \qquad \mu = \bar{\mu} \quad \text{on } \Gamma_c; \tag{21}$$

and the natural boundary conditions are

$$\nabla c \cdot \mathbf{n} = j_c \quad \text{on } \Gamma_d; \qquad \nabla \phi \cdot \mathbf{n} = j_\phi \quad \text{on } \Gamma_e; \qquad \nabla \mu \cdot \mathbf{n} = j_\mu \quad \text{on } \Gamma_f. \tag{22}$$

The initial conditions are

$$c|_{t=0} = c_0; \qquad \phi|_{t=0} = \phi_0; \qquad \mu|_{t=0} = \mu_0; \qquad \text{in } \Omega. \tag{23}$$

For dendritic growth simulation, we specify the domain size as 960 and the radius of the initial seed as $R_0 = 8$. The boundary conditions impose no flux at the bottom and lateral boundaries and Dirichlet boundary condition $\bar{c} = -\Psi$ at the top boundary as a far-field concentration. We initialize the whole domain as the supersaturated liquid phase with $\phi_0 = -1$ and $c_0 = -\Psi$, except the half-circular seed as the solid phase with $\phi_0 = 1$ and $c_0 = -\Psi$. We impose a smooth transition from the solid to liquid phases using the following half-circular seed.

$$\phi(r) = \left[1 - \tanh \frac{|r| - R_0}{\sqrt{2}}\right] - 1 \tag{24}$$

Based on the governing equations (16)-(18) and corresponding boundary and initial conditions (21)-(23), we derive weak formulations of dendritic growth in the Appendix 7, where time marching is the forward Euler method and space discretization is the finite element method. And then we implement these weak forms in an open-source high-performance phase-field code, PRISMS-PF DeWitt et al. (2020), which allows us to use adaptive mesh refinement and matrix-free technique to reduce computation cost.

2.4 Fractal dimension as an internal-energy-evolution proxy

The box-counting method is here used to measure the fractal dimension (FD) of the dendrites. FD is an intrinsic characteristic of fractals introduced by Mandelbrot (1982) to characterize a structure with self-similarity at all scales. The growth of dendrites is a remarkable fractal pattern in nature. Here, we use FD to quantitatively distinguish dendrites that grow out from different environments. The box-counting method we have implemented for measuring FD of dendrites expresses as follows (Vicsek, 1992):

$$\mathrm{FD} = \lim_{r \to 0} \frac{\log N(r)}{-\log r} \tag{25}$$

where $N(r)$ is the number of boxes that cover the structure and r is the box size.

We estimate FD by plotting $\log N(r)$ versus $\log r$ with the change of the box size r. The curve is linear and the absolute value of its slope corresponds to the value of FD. The box-counting algorithm of Moisy (2008) is implemented in Matlab, capable of coping with both 2-D binary and RGB color images. The procedure to measure FD of the dendrites from our simulation or the photograph has the following three steps:

(i) the code reads a binary image or processes a color image to grayscale C, where the gray value of the dendrite is equal to 0 (white), while the gray value of the background is set to 1 (black);
(ii) we select a region containing dendrites (gray value = 1);
(iii) the code recursively calculates $N(r)$ (box number) by decreasing r (box size);
(iv) the code draws the curve of $\log N(r)$ versus $\log r$ and estimates the FD and its standard error.

In the third step (iii), we can select the upper and lower limits of the box size r in the following manner. The box sizes we use follow powers of 2, i.e., $r = 1, 2, 4, \ldots, 2^p$. The lower limit is the binary size of 1, whereas the upper 2^p is limited by the size of the gray matrix C. The specific condition is p should be the smallest integer such that the bigger size of the matrix C in columns and rows satisfies $C \leq 2^p$. In the case of the sizes of C smaller than 2^p, the code ensures the matrix C to pad with 1 to approach size 2^p (e.g., a 560-by-720 picture is padded to 1024-by-1024). This enables the process of arbitrary sizes of images with little effort. Furthermore, for an RGB color image with a matrix of m-by-n-by-3, the code first sums up the 3 RGB planes.

3 Results

We now study numerically the behavior of the phase-field model of Section 2. We implement the weak forms in PRISMS-PF, an open-source phase-field modeling framework (DeWitt et al., 2020). First, we study the method's convergence in space and time in Section 3.1. Next, we characterize the observed and simulated dendrites by a general criterion involving a visual and quantitative distinction in Section 3.2. Then, we perform parameter studies on supersaturation and diffusion coefficients to explore different dendritic patterns, including solute diffusion and phase-field (Allen-Cahn) diffusion coefficients in Section 3.3. Finally, we reproduce the classified dendrites observed on rock surfaces by comparing the morphology classification and measuring the fractal dimension in Section 3.4.

3.1 Model convergence study

We demonstrate the reliability of PRISMS-PF for dendritic growth simulation by conducting a convergence study regarding the mesh and time-step sizes. Figure 4 gives geometry information and the detailed initial and boundary conditions. Table 1 lists the model parameters for the numerical test. We use cubic finite elements to capture the highly

nonlinear and time-dependent dendritic growth, which outperforms a finite difference method with five points across the interface (DeWitt et al., 2020).

Table 1. Model parametrization for dendritic growth

Parameter	Symbol	Value
Interfacial thickness	W_0	1.0
Diffusion coefficient	D	100
Anisotropic symmetry order	m	10
Anisotropy strength	ϵ_m	0.05
Offset angle	θ_0	0
Relaxation time	τ	1.0
Supersaturation	Ψ	0.3

We investigate the effect of the ratio of the length scale represented by W_0 with the mesh size h to carry out a spatial convergence study. We fix the length scale $W_0 = 1.0$ related to the interfacial thickness but progressively refine the mesh with different refinement levels. We reduce the computational cost by adaptively refining the mesh every five-hundred time steps from an initially uniform mesh (level=3) to the maximum refinement levels. We adopt a simple adaptive mesh refinement criterion, which refines cells where the absolute magnitude of the phase-field variable is less than 0.99. Meanwhile, the refined cells are coarsened when the absolute magnitude ϕ is above 0.99. Here, we set the maximum levels of refinement equal to 6, 7, 8, and 9, resulting in the ratio $W_0/h_{\min}$ ranging from 0.2 to 1.6. As we use the explicit time scheme, we select a small time increment $\Delta t = 5{\times}10^{-5}$ to satisfy the Courant–Friedrichs–Lewy condition (CFL) condition for all the mesh sizes. Both qualitative and quantitative analyses are conducted to compare between different tests.

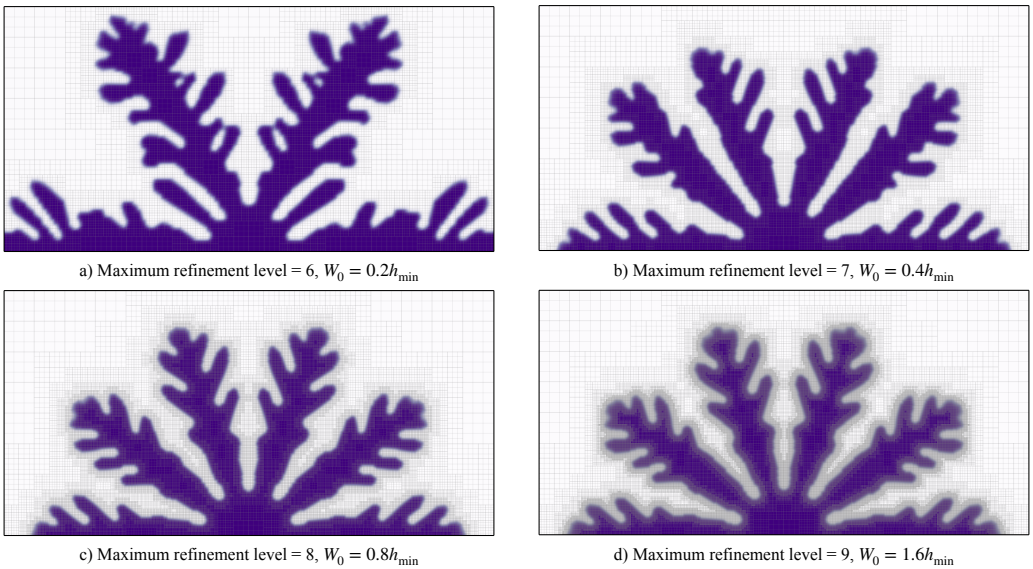

Figure 5. Convergence of ϕ shape as mesh is refined for a) $W_0 = 0.2h_{\min}$, b) $W_0 = 0.4h_{\min}$, c) $W_0 = 0.8h_{\min}$ and d) $W_0 = 1.6h_{\min}$ in the domain of $x \in [320, 640]$ and $y \in [0, 160]$.

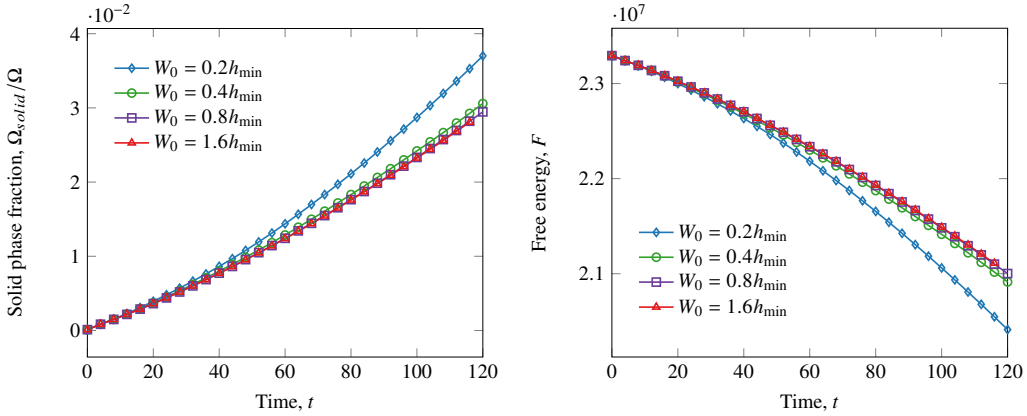

(a) Solid phase fraction evolution (b) Free energy evolution

Figure 6. (a) Solid phase fraction & (b) free energy evolution for different ratios of $W_0/h_{\min}$

Figure 5 shows the dendritic patterns for different maximum levels of refinement at the end of simulation $t = 80$; these results demonstrate the effect of the ratio $W_0/h_{\min}$ on the dendritic growing process. The simulated patterns converge towards a consistent shape as the ratio $W_0/h_{\min}$ increases; when the value $W_0/h_{\min} \geq 0.8$ corresponds to the maximum levels ≥ 8, we observe spatial convergence.

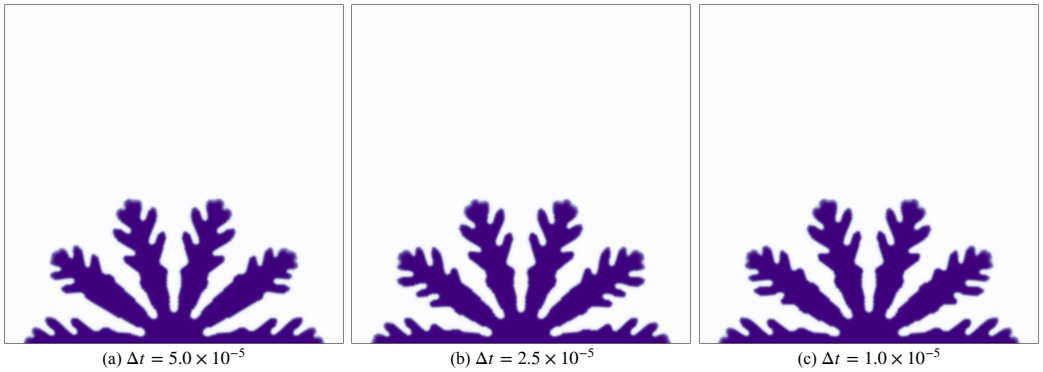

(a) $\Delta t = 5.0 \times 10^{-5}$ (b) $\Delta t = 2.5 \times 10^{-5}$ (c) $\Delta t = 1.0 \times 10^{-5}$

Figure 7. Convergence of ϕ shape as the time increment takes values of (a) $\Delta t = 5.0 \times 10^{-5}$, (b) $\Delta t = 2.5 \times 10^{-5}$, and (c) $\Delta t = 1.0 \times 10^{-5}$ in the domain of $x \in [320, 640]$ and $y \in [0, 320]$.

Next, we quantitatively compare the temporal evolution of the free energy and solid phase fraction (i.e., ratio of solid phase to the sum of the two phases): Ω_{solid}/Ω in the domain. Figure 6 shows that the temporal evolution of the solid phase fraction and free energy is off when $W_0/h_{\min} < 0.4$. Nevertheless, beyond this ratio (e.g., $W_0/h_{\min} \geq 0.8$), the free energy and solid phase fraction curves are almost indistinguishable. In the literature, a typical value $W_0/h_{\min}$ ranging from 2 to 4 (Karma & Rappel, 1998; Z. Xu & Meakin, 2011; Peco et al., 2019; Kundin & Steinbach, 2019; Ghanbari et al., 2020) is recommended for phase-field modeling structure evolution. However, we find that a lower level of refinement is sufficient to guarantee convergence in our simulations, which could be related to the high-order (cubic) elements we use, instead of linear elements in the reference (DeWitt et al., 2020; Bhagat & Rudraraju, 2022). Thus, we use cubic elements

and select a ratio of the length scale to the minimum mesh size $W_0/h_{\min}$ ranging from 0.8 to 1.6.

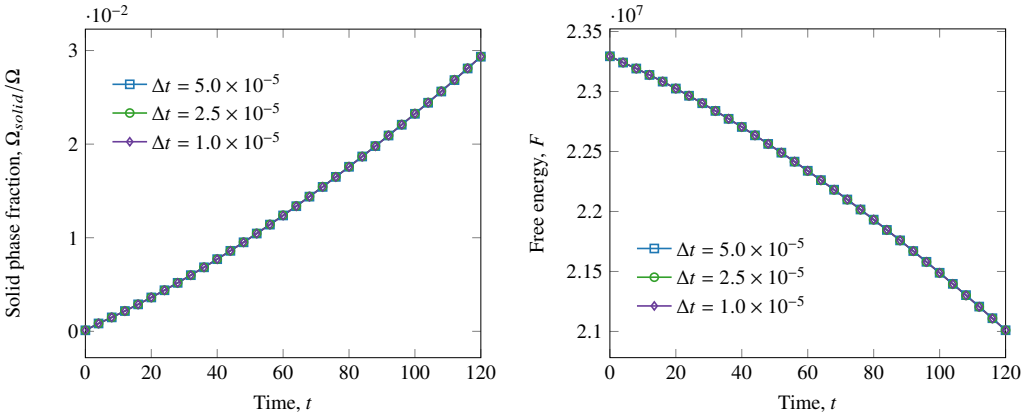

(a) Solid phase fraction evolution

(b) Free energy evolution

Figure 8. (a) Solid phase fraction & (b) free energy evolution for different time step sizes

Next, we study the temporal convergence of our discretization. We set the discretization ratio to $W_0/h_{\min} = 1.6$ with the time step $\Delta t = 5 \times 10^{-5}$ as a reference. Then, we reduce the time steps to $\Delta t = 2.5 \times 10^{-5}$ and 1×10^{-5}, respectively. We compare the simulated dendritic pattern, the solid phase fraction, and the free energy with the preferred results. Figure 7 depicts the convergence of results for time steps. The reduced time steps are in excellent quantitative agreement with the reference case in terms of the solid phase fraction and free energy as Figure 8 illustrates. These results demonstrate the time increment $\Delta t = 5 \times 10^{-5}$ is sufficiently small to ensure convergent results. Therefore, we select the time increment $\Delta t = 5 \times 10^{-5}$ for this study.

3.2 Dendritic morphology classification

First, we characterize how the observed patterns can be classified since the formed pattern evolving from a small nucleus is diverse (Brener et al., 1996; Lin et al., 2022). Based on the classifications available in literature we propose a qualitative morphology diagram as illustrated in Figure 9 for the dendrite patterns produced by mineral precipitation reactions. Figure 9 compares the three pattern categories, containing needle-, tree-, and seaweed-like dendrites, to the corresponding numerical results with varying input parameters. For a detailed description of parameters for the simulated patterns see Section 3.3. We define the three types of dendritic patterns in the following way:

Needle-like dendrites: This dendritic morphology propagates in a preferred direction, controlled by the anisotropy index m in Eq. (10). This pattern is dominated by primary (fin) branches without or with the under-developed secondary (or side) branches, see Figure 9(a). The formed needle-like pattern is rather simple and the side branches rarely emerge, thereby resulting in a relatively small fractal dimension.

Tree-like dendrites: This dendritic morphology develops symmetrically and grows with well-defined side branches, as Figure 9(b) shows. Two main characteristics describe this pattern: (i) the side branches frequently appear on each primary fin and (ii) the thickness of the side branches is comparable to that measured by primary branches. The formed morphology has an intermediate fractal dimension compared to the others.

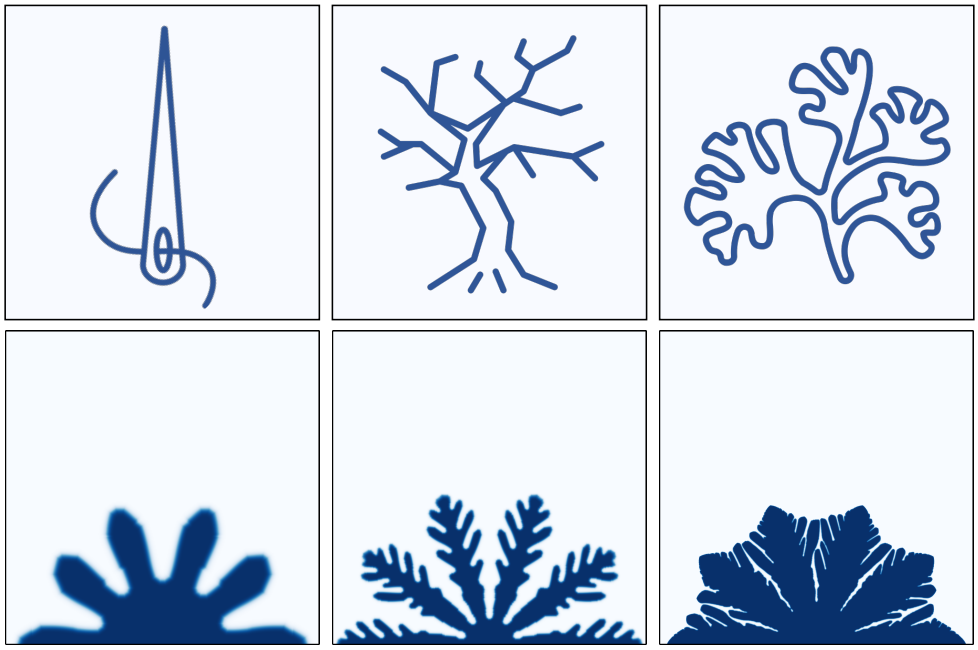

(a) Needle-like dendrites (b) Tree-like dendrites (c) Seaweed-like dendrites

Figure 9. Comparison of the classical morphologies sketches and simulated patterns: (a) needle-like dendrites, (b) tree-like dendrites, and (c) seaweed-like dendrites.

Seaweed-like dendrites: The seaweed morphology has a denser structure with a relatively large tip radius as Figure 9(c) shows. Also, the growth of primary branches may impede each other, causing a lack of symmetry in the shape. A prominent feature of this pattern is that its primary arms are thicker than its side branches. The dense primary branches reduce the branch spacing and, therefore, result in a larger seaweed fractal dimension.

This simple dendritic morphology classification enables us to visually distinguish the patterns observed in the field, for example as described for the manganese dendrites in (Ng & Teh, 2009).

3.3 Parameter space analysis and morphologies

In Section 3.2, we define three particular types of dendritic morphologies, namely needle-, tree-, and seaweed-like dendrites. Now we conduct a comprehensive parameter study to identify the main parameters that control the selection of patterns. We evaluate the associated parameter ranges in which a specific morphology emerges. Our numerical results suggest that the morphology selection of dendritic growth depends on three parameters. The first number is the supersaturation level Ψ and the two others are the diffusion coefficients in Eq. (14) (i.e., W_0^2/τ_0) and Eq. (15) (i.e., D). We define

$$G = W_0^2/\tau_0$$

as the phase-field diffusion coefficient. Following (Karma & Rappel, 1998), we assume the kinetic coefficient τ_0 has the value of 1. Thus, the phase-field diffusion coefficient G is solely controlled by the interfacial thickness coefficient, as W_0^2.

We explore the parameter spaces in detail to better understand the effect of these parameters on the pattern formation of dendrites. By fixing one control parameter and

varying the other two parameters, we obtain a phase morphology diagram of the dendritic patterns. We thereby first qualitatively classify them into the three dendritic morphologies from our simulation results. Then, we quantitatively evaluate the patterns by their fractal dimensions using the box-counting method (see Section 2.4). The simulation results presented here are based on the model convergence study detailed in Section 3.1.

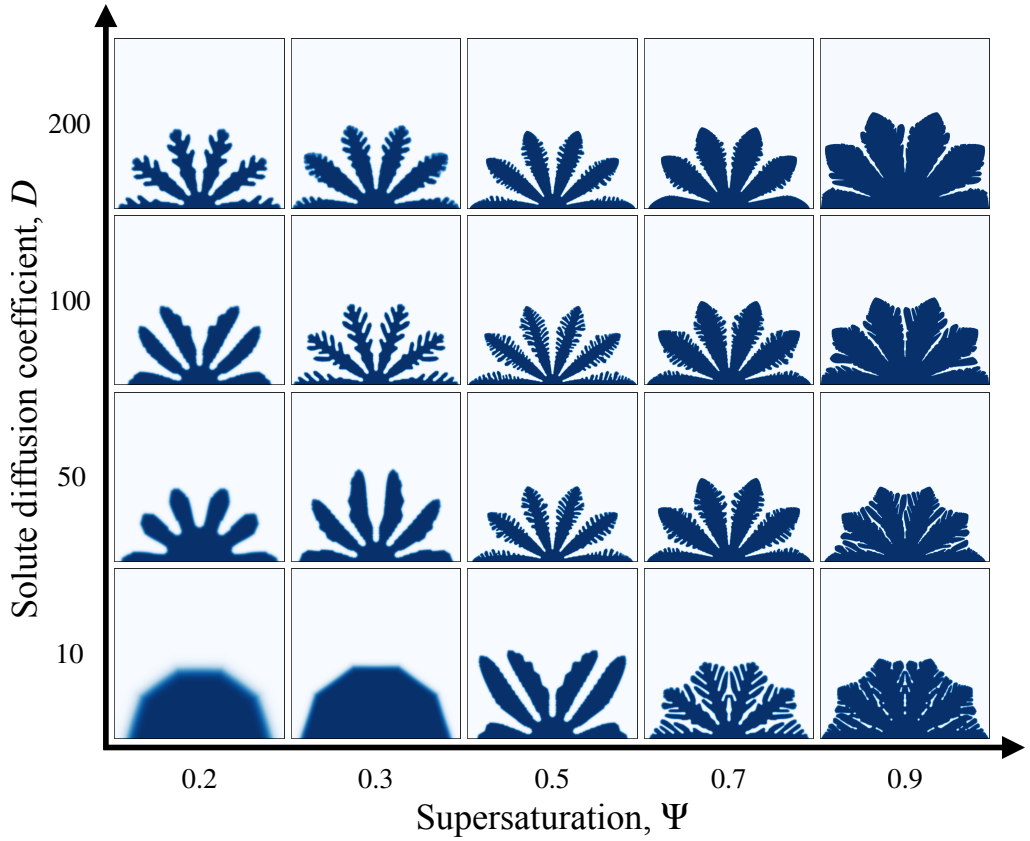

Figure 10. Morphology evolution in the supersaturation and diffusion phase diagram

3.3.1 Influence of supersaturation and solute diffusion coefficient

We assess numerically the influence of the supersaturation Ψ and solute diffusion coefficient D on the evolution of the dendritic patterns by sampling a range of values for Ψ and D. For this parameter sweep, we keep the phase-field diffusion coefficient $G = 1.0$ corresponding to the interfacial thickness $W_0 = 1$ fixed so that morphology selection is solely driven by variations in Ψ and D. We select the supersaturation as 0.2 and 0.3 to 0.9 with 0.2 increments, which satisfy the limit of $\Psi \leq 1$. Also, we set the solute diffusion coefficient to 10, 50, 100, and 200. Therefore, we obtain the dendritic morphology evolution with varying Ψ and D using 20 simulations, as presented in Figure 10.

In all the presented simulation results hereafter, we select each overall simulation time based on achieving roughly the same pattern size. In this phase morphology diagram, the three dendritic growth types (see Section 3.2) for different Ψ-D combinations are identified. The generated patterns are classified (based on the earlier described dendritic morphology classification criterion) into seaweed-like dendrites, tree-like dendrites,

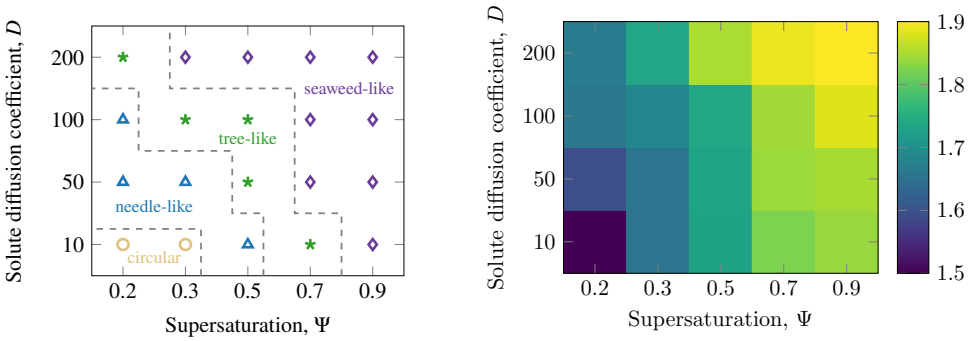

(a) Dendrites classification

(b) Fractal dimension

Figure 11. Dendritic-morphology phase diagram: supersaturation & solute diffusion. (a) dendrites classification according to Section 3.2 criterion and (b) fractal dimension heatmap. Gray dashed lines separate circular, needle-, tree-, and seaweed-like patterns.

needle-like dendrites and no dendrites (circular) as shown in Figure 11(a). Based on the pattern selection in the horizontal axis, we find a sufficiently large Ψ is able to change the generated structure shape from any type to seaweed-like dendrites, independent of the value of D.

The solute diffusion coefficient D also plays a significant role in determining the dendritic growth type, and the pattern selection is relevant to the supersaturation level, as shown in Figure 11(a). When the supersaturation level is low, with an increasing solute diffusivity, the transition from needle-like to tree-like dendrites occurs. Under a supersaturation of 0.5, a full-spectrum transition from needle-like to tree-like to seaweed-like dendritic growth takes place. With a supersaturation level, the growth patterns reduce to tree-like and seaweed-like dendritic morphologies.

Although the dendritic classification shown in Figure 11(a) is direct and intuitive, a quantitative description is desired for the generated dendritic morphology. FD by box counting is hence employed to refine the dendritic morphology characterization, as shown in Figure 11(b). A general trend observed from Figure 11(b) is that the fractal dimension of the generated dendritic patterns increases as Ψ and D grow. Since a combination of larger Ψ and D produces more arms (i.e., side branches) and thicker primary branches, the morphology appears to be more complicated. Within one category of the dendritic type, the fractal classification allows us to have a refined view of the morphological characteristics. For example, for the cases of $D = 100$ with Ψ =0.3 and 0.5, both fall into the tree-like classification, while the value of FD, 1.68 and 1.74, respectively, provides a quantitative description of the primary precipitated structure versus the secondary precipitated structure.

3.3.2 Influence of phase-field and solute diffusion coefficients

In this section, we study the effect of the phase-field describing the interface and the solute diffusivity on dendritic pattern formation. Similarly as in Section 3.3.1, with a fixed value of supersaturation at 1.0 we set the solute diffusion coefficient D consistent with Figure 10 while varying the phase-field diffusion coefficient G by altering the interfacial thickness coefficient W_0. We set W_0 to 0.5 to 1.0 with a 0.1 increment, such that our simulations satisfy the convergence condition $W_0/h_{\min} \geq 0.8$. The simulation results suggest that a smaller value of W_0 slows down the transition between different types of pattern formation. Lower W_0 values are not explored here as the three repre-

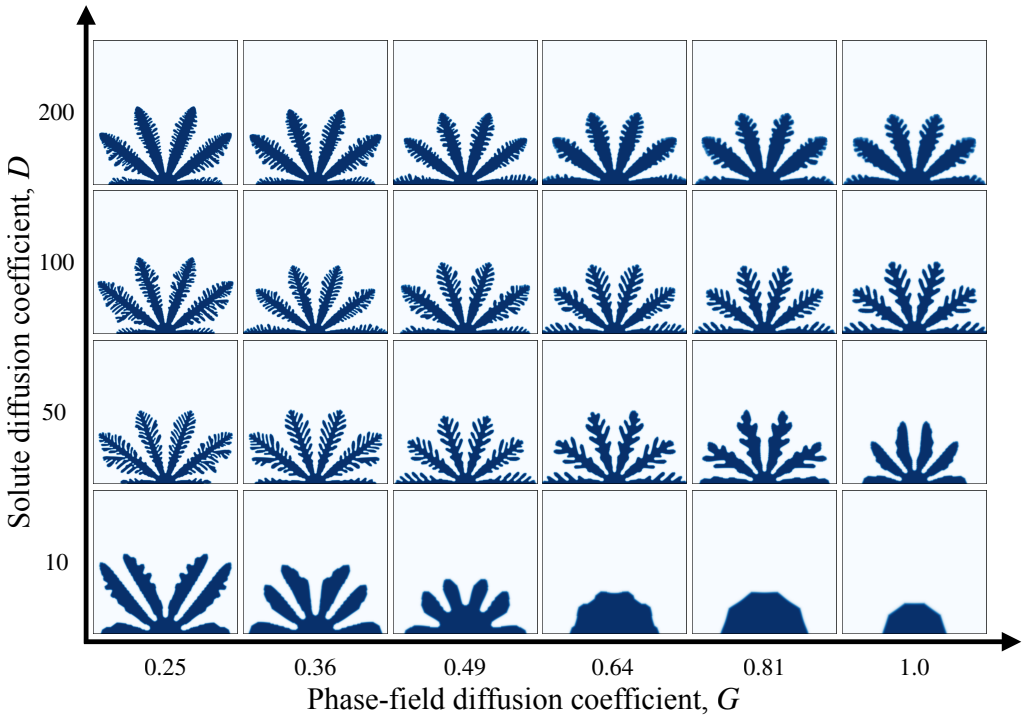

Figure 12. Morphology evolution in the interfacial thickness & diffusion phase diagram

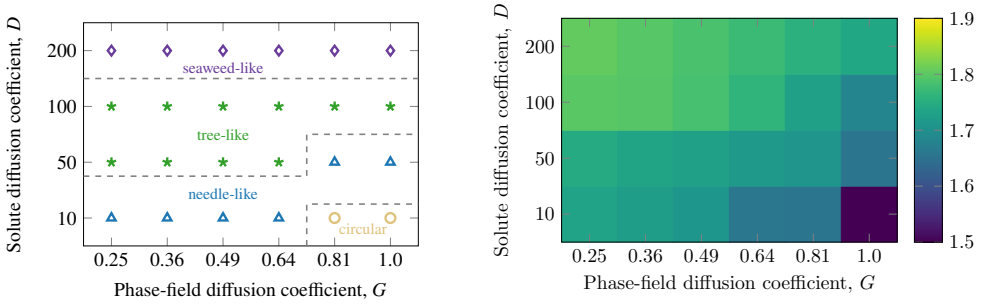

(a) Dendrites classification

(b) Fractal dimension

Figure 13. Dendritic-morphology phase diagram: interfacial thickness & solute diffusion. (a) dendrites classification according to Section 3.2 criterion and (b) fractal dimension heatmap. Gray dashed lines separate circular, needle-, tree-, and seaweed-like patterns.

sentative dendritic morphologies can already be captured with the selected range of parameters.

Figure 12 presents the dendritic morphology evolution in the interfacial phase-field and solute diffusivity space demonstrating two dominant effects. First, the simulated patterns from right to left show that G controls the number of side branches, i.e., as G drops, the branching increases reducing the interval between the side branches. With the increase of the number of the side branches (secondary precipitated structure) on a primary branch, the dendritic morphology transitions from simple patterns to more complex ones, with pattern classification presented in Figure 13(a). For example, a needle-like dendrite changes to a tree-like pattern when the phase-field diffusion coefficient decreases from 0.81 to 0.64 for solute diffusivity $D = 50$. Additionally, as the branching

increases the secondary precipitated structure becomes denser without noticeable shortening, thus causing an increase in the fractal dimension of the growth pattern. This tendency is quantitatively depicted in Figure 13(b) for different solute diffusion coefficients. Second, how fast the solute diffuses influences the dendritic morphology, i.e., the dendrites become more complex as the solute diffusion coefficient D increases. A low value of $D = 10$ promotes the formation of needle-like structures, while a high diffusivity $D = 200$ leads to seaweed-like dendrites regardless of the phase-field coefficient. Intermediate range of the solute diffusivity tends to pick up on the tree-like dendritic morphology, as shown in Figure 12. The effect of solute diffusivity on the pattern selection of dendritic growth is quantitatively described by the fractal dimension in Figure 13(b).

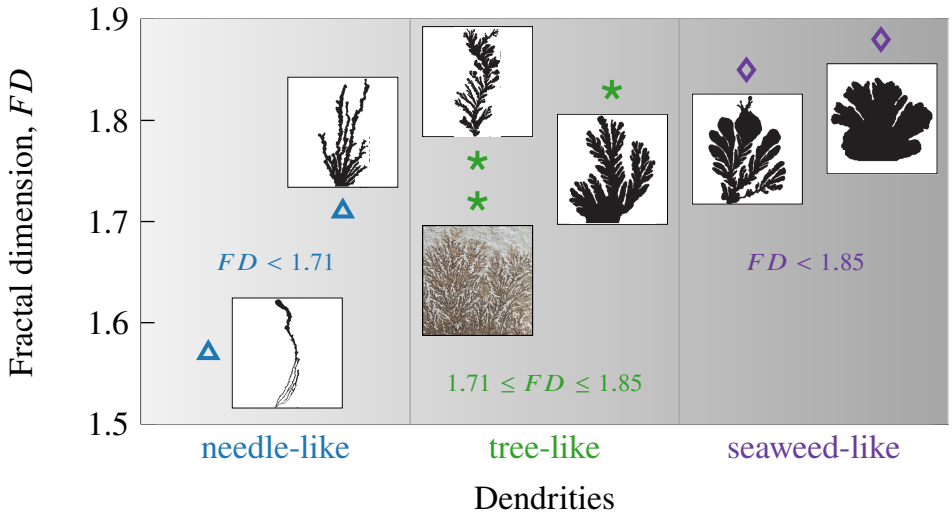

Figure 14. Manganese dendrite classification & fractal dimension calculation. The colored image is from Solnhofen limestone, while others are from (Ng & Teh, 2009). Vertical solid lines indicate the crossover between needle-, tree-, and seaweed-like dendrites.

3.4 Dendritic morphology in rocks

In this section, we employ our model to capture dendrites that are precipitate by reaction-diffusion processes in minerals, in particular manganese dendrites. We use the results of the previous section to invert the corresponding parameters, especially solute diffusion coefficient D, for specific dendritic patterns. We combine a qualitative and quantitative method and separate the whole procedure into three steps. First, we classify the real-world (field) dendrites reported in the literature into three categories based on the criterion in Section 3.2. Second, we qualitatively compare each field dendrite with our simulation results and find resembling dendritic morphology. Finally, we measure the fractal dimension FD of these dendrites to find a comparable FD to the field dendrite.

3.4.1 Field dendritic morphologies: classification & fractal dimension

Before comparing simulation and field dendrites, we categorize the dendrites emerging on rock interfaces. In the present work, we consider manganese dendrites as an appropriate candidate for two reasons. First, they commonly grow along geological discontinuities, like joints, cracks, and fractures, and appear on surfaces of different rocks, such as limestone (Chopard et al., 1991), quartz (Ng & Teh, 2009) and magnesite ore (Merdan & Bayirli, 2005). In addition, the individual manganese dendrites show various morpholo-

gies that range from simple shapes with few branches (none in some cases) to complex intricately branched patterns. Herein, we analyze two series of mineral dendrites. The first one shows six distinct patterns obtained from vein quartz in Northern Kuala Lumpur (Ng & Teh, 2009). The second one uses our field photographs of well-documented manganese dendrites in Solnhofen limestone (Chopard et al., 1991).

Figure 14 shows from left to right two series of manganese dendrites and groups them into three different categories. The manganese dendrites on vein quartz have visually distinct patterns with two samples in each class, while one commonly observed in limestone shows a tree-like shape. We further differentiate them by plotting the fractal dimension FD reported by Ng and Teh (2009), see Figure 14 from bottom to top. We also measure our Solnhofen limestone sample using the box-counting method as FD=1.72, which is comparable to that estimated by (Chopard et al., 1991) FD$\approx$ 1.75 in the same region. The seaweed-like dendrites with broad and short branches, in general, have larger FD, compared to needle-like ones with long and thin branches; while the FD number of tree-like dendrites is intermediate. We explicitly divide the dendritic morphologies into three types based on our findings; we assume the needle-like dendrite has an FD below 1.71, while the FD of the seaweed-like dendrite is above 1.85, the seaweed-like dendrite's FD ranges from 1.71 to 1.85.

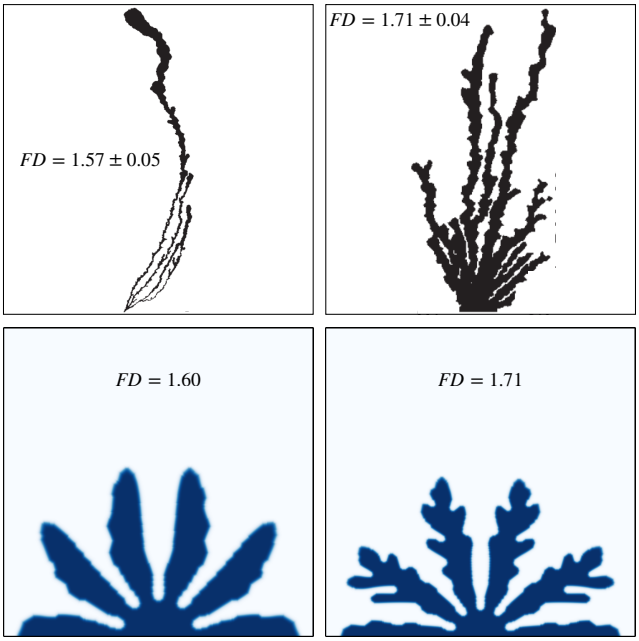

Figure 15. Comparison of needle-like dendritic morphologies and simulated patterns

3.4.2 Dendritic morphology comparison

Seeking to decipher which parameter controls the field dendritic morphologies, we compare studies for each type of dendrite classification in this section.

Needle-like dendrites: We begin with the simplest dendritic pattern with fewer side branches in the needle-like category. Figure 15 shows two dendrites with different fractal dimensions. Although the side branches of both dendrites are underdeveloped, the one with smoother primary branches has a smaller FD=1.57. First, we explore two morphology diagrams from Sections 3.3.1 and 3.3.2 and search for similar dendritic shapes. In Figure 12, we find two resembling dendritic morphologies. In these simulations, the

solute diffusion coefficient is $D = 50$, while the phase-field diffusion coefficients are $G = 0.81$ and 1.0, respectively. Figure 15 illustrates the similarities between the simulated and field dendrites. Overall, the simulated dendritic growth resembles field observations except for the irregular growth directions in the real-world dendrites (see also the tree- and seaweed-like dendrites). The irregular change in the growth direction in the field may be caused by material heterogeneities and the complex hydrogeological environments where these dendrites evolve; nevertheless, introducing a noise term to our computational model (Karma & Rappel, 1999) to approximate these effects is beyond the scope of our study. Furthermore, we quantitatively compare the fractal dimension between the real dendrites from the field (Ng & Teh, 2009) and our simulations in Figure 13(b). Our simulation results are in good agreement with the field observation. For example, smoother dendrites result in FD=1.60 compared to 1.57±0.05 in the field; similarly, the relatively rough dendrites have FD=1.71 in the range of 1.71 ± 0.04.

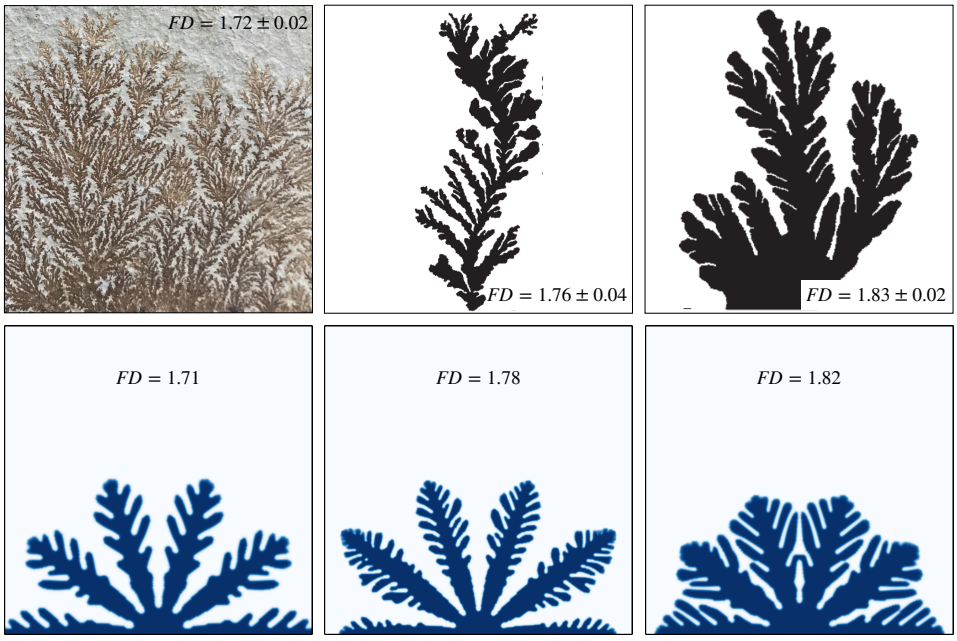

Figure 16. Comparison of the tree-like dendritic morphologies and simulated patterns

Tree-like dendrites: The tree-like dendritic growth is a commonly observed dendrite in different disciplines. Following the procedure of the above comparison, we identify the corresponding dendritic shapes similar to the field tree-like dendrites in Figure 16. The manganese dendrites from Solnhofen limestone have a smaller FD=1.72 compared to that observed on vein quartz FD=1.76 and 1.83. As for the dendrites in Solnhofen limestone, parameters $G = 1$ and $D = 100$ give a similar pattern and a similar FD number in Figure 13(b). With the phase-field diffusion coefficient decreasing to $G = 0.49$ with fixed $D = 100$, our simulation results in a dendritic pattern observed in quartz. For this simulation, several side branches tend to experience a coarsening process and generate thick side arms, causing more regions to be filled with the manganese mineral as Figure 16 illustrates. The filling ratio increment of the minerals ensures an increase in fractal dimension. Regarding the higher FD=1.83 case, the dendrites show a relatively broad structure and its side branches are comparable to the main branches. We obtain this kind of dendritic morphology by increasing the saturation level to $\Psi = 0.7$ and dropping the solute diffusion coefficient to $D = 10$ as Figure 10 shows. The estimated FD=1.82 matches well the quantity 1.83 ± 0.02 reported by Ng and Teh (2009).

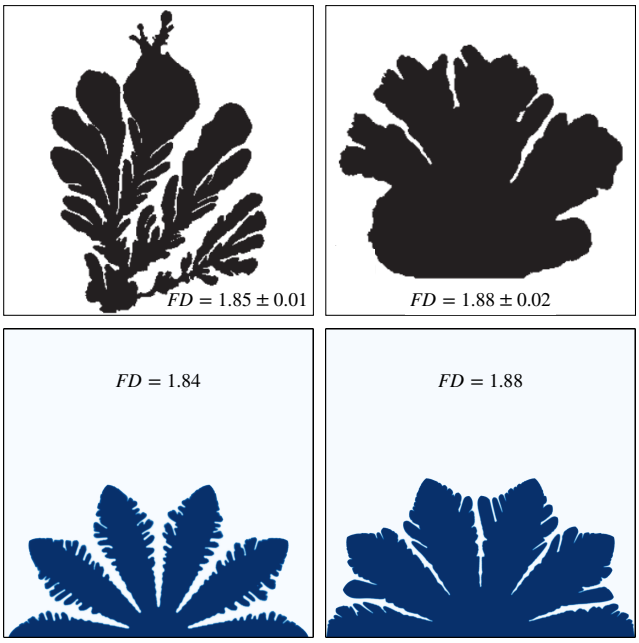

Figure 17. Comparison of the seaweed-like dendritic morphologies and simulated patterns

Seaweed-like dendrites: Next, we analyze the most complex structures: seaweed-like dendrites. Compared to the thick arms in the tree-like dendrites related to the coarsening processing in Figure 16, the complex dendrites in Figure 17 are likely associated with a higher manganese concentration environment. We verify this hypothesis by increasing the initial supersaturation level in our simulations. Interestingly, as the supersaturation level Ψ grows, the dendritic morphologies become denser and fuller structures. With the solute diffusion coefficient $D = 100$, the supersaturation level of $\Psi = 0.7$ and 0.9 generates two dendritic morphologies comparable to the field observations, see Figure 17. Our simulations have good agreement in FD numbers; they are FD=1.84 and 1.88 compared to the field observations in the range of 1.85 ± 0.01 and 1.88 ± 0.02, respectively.

4 Discussion

The selection and formation of two distinct precipitation patterns (i.e., Liesegang rings versus dendritic growth) in the same rock formation (Solnhofen limestone) has been suggested to be caused by a common reaction-diffusion process (Chopard et al., 1991). However, the original proposition was found to be not appropriate as it does not reproduce time- and length scales of Liesegang rings. Here, we find that the difference between the two processes is the fundamental mode of mass transfer of the reactant (conserved versus non-conserved) suggesting that the underlying mechanisms are stemming from different driving forces for the supersaturated fluid mass movement in the reaction-diffusion processes. Accordingly, a slow process would allow the replenishment of the dissolved reactant while a fast flow would result in a depletion of the reactant in the solvent.

A recent inversion scheme for the Liesegang phenomenon based on field photos (Liu et al., 2022) uses the Cahn-Hilliard equation where the phase-field variable is a conserved quantity. The approach is based on an energy formulation using a double well potential, where the separation between two species is formed through attraction to the minima of the double well. This formulation can be compared to the classical supersation model

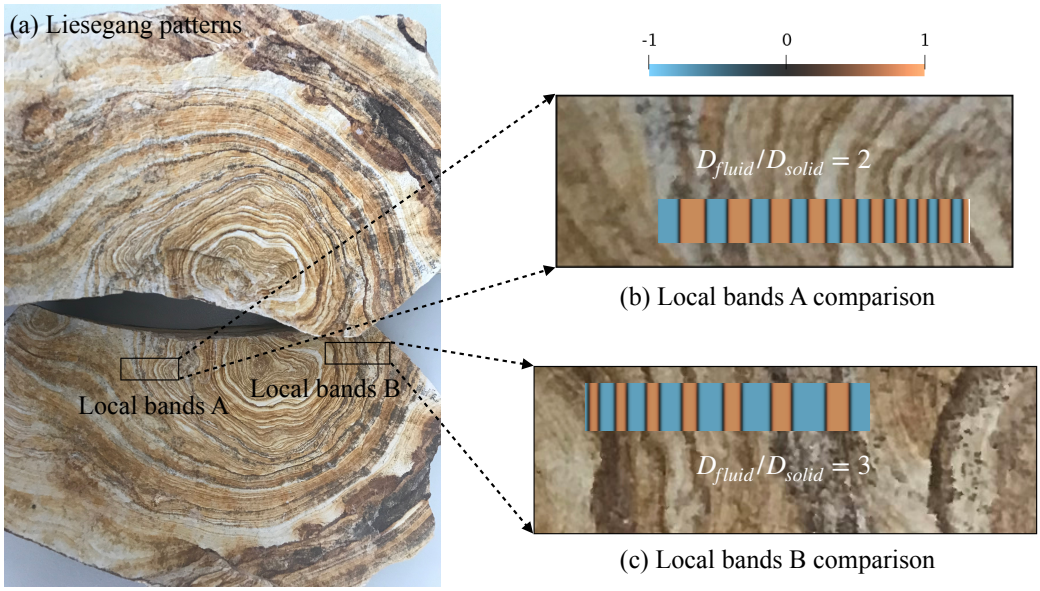

Figure 18. (a) Two local Liesegang patterns in Solnhofen limestone and local Liesegang bands comparison: (b) local bands A and (c) local bands B with their numerical results. Scaled parameters for both simulations are $\bar{a} = 100$, $a_0 = 0$, $m_0 = -1.5$, $D_b = 1.0$, $\kappa = 1.0$, $\varepsilon = 1.0$, $\gamma = 0.15$, $\sigma = 0.2$, and $\eta_c = 0$, except $b_0 = 1.0$ and $D_a = 2$ for the local bands A while $b_0 = 0.75$ and $D_a = 3$ for the local bands B. For parameter definitions refer to (Liu et al., 2023a).

with a threshold (e.g. (Ostwald, 1902; Steefel & Maher, 2009)) by identifying the energy barrier separating the two minima as equivalent threshold. The inversion of the diffusion coefficient from field photographs was performed on an archetype banded rock formation, the Zebra rock formation of Western Australia. The simulations showed that a low solute diffusion coefficient in fluid flow is capable of forming Liesegang structures (Liu et al., 2022). The models suggest that a slow viscous material flow through a tight formation, presumably supported by mechanical-hydrological-chemical forces, is causing growth of the Liesegang pattern which form as a pervasive pattern through the sedimentary layering.

For verifying the hypothesis that follows from the observation that dendritic growth is associated with the subsurface fluid flow along the geological discontinuities and sedimentary laminations, we compare the resulting diffusivities from the dendrites versus a fit to the observed Liesegang rings in Solnhofen limestone shown in Figures 1 and 18.

The inversion of the ratio of solid over fluid diffusivity follows from a conversion of the approach in our earlier work (Liu et al., 2023a) from a Cartesian- to a Cylindrical coordinate system. The observed rings in Figure 1 are irregular suggesting heterogeneities that affected their growth. We select two areas that have minimal material perturbations for the fitting diffusion coefficients. Our analysis confirms the findings for the Cartesian Liesegang patterns in Zebra rock. The Liesgang phenomenon in Solnhofen limestone is also triggered by a fluid diffusion coefficient that is on the same order of magnitude (i.e., 2 to 3 times faster than the solid diffusivity defined by the viscous deformation of the matrix), see Figure 18.

This finding supports that a common formation mechanism for Liesegang rings is stemming from a driving force for the solute transport (like Mn- or Fe-bearing acidic fluid) which is either an extremely slow flux induced by an (electro-)chemical potential differ-

ence or a slow mechanically forced fluid flow caused by a stress gradient, e.g. compaction from overburden stress or tectonic forces (Liu et al., 2023a), or a combination thereof. Liesegang rings consequently can form independent of the primary high permeability interbed layers or secondary crack interfaces that control dendrites. Due to mass conservation they must form in a direction perpendicular to the primary thermodynamic force which in the mechanical case is the direction of compaction of the sedimentary layer triggering the formation of Liesegang rings.

For a sedimentary compaction environment, Liesegang rings are expected to form as a pervasive structure through the sedimentary layering. This is confirmed by the identical pattern observed on the front and reverse sides in Figure 1. The sample incorporates multiple sedimentary layers of the fine-grained mud-and silt limestone Solnhofen limestone which sedimented and compacted in an oxygen poor environment. During subsidence the layers were compressed and conserved multiple macrofossils, such as the complete skeleton, including the feathers of the primeval bird (Archaeopteryx), flattened in its bedding planes. The fine grain size and the high mud- and silt content suggest low primary permeability across the sedimentary layers during the compaction process which is consistent with our finding of low solute transfer.

In contrast, the formation of dendrites shows, on average, relatively large solute diffusion coefficients; see Section 3.4.2. The high diffusion coefficient seems associated with the flow of subsurface fluid driven by a fluid pressure gradient driven by hydraulic forcing. The pressure difference is able to push the Mn- and Fe-bearing fluids to invade sedimentary discontinuities with a rather high diffusivity and consequently leads to the mineralisation of dendritic-shaped structures. Qualitative analyses also result in similar consequences for the mineral dendrite-forming process by observing the images from experiments or fields (Ng & Teh, 2009; García-Ruiz & Otálora, 2015). Our numerical simulations confirm this hypothesis quantitatively and provide an inversion tool for the dynamic coefficients from static snapshots of the rock patterns.

Parameter studies are required to model the wide variety of dendritic morphologies observed on rock surfaces. The key parameters controlling the transition between different types of dendritic patterns are of particular interest to the community. We find that three control parameters play an essential role in determining the dendritic growth morphology: supersaturation, solute diffusion, and phase-field diffusion coefficient. Specifically, the supersaturation and solute diffusion coefficient have similar effects. As the supersaturation or solute diffusion coefficient grows the resulting dendritic branches are denser and broader. The Mullins-Sekerwa instability (Mullins & Sekerka, 1963) justifies this observation. An initially small perturbation (bump) can grow faster in an environment with higher supersaturation or diffusivity, which results in a larger mass flux from the surrounding medium. More flux leads to faster growth that in turn leads to a sharper bump which collects more flux (Karma & Rappel, 1998; Langer, 1980). Additionally, the sharper interfaces result in larger fractality and complex structures. However, seaweed-like dendrites require a high supersaturation level to have fuller and denser structures. This is because the high supersaturation makes continuous growth dominate the whole process and makes the surface become rounded, thereby causing a dense and full structure (García-Ruiz & Otálora, 2015).

Alternatively, the high Allen-Cahn phase-field diffusion coefficient reduces the pattern complexity by decreasing the side branches' growth. The reason is that the value is associated with the solid-liquid interface effects, such as anisotropy, surface tension, and surface kinetics tension, which usually stabilize the dendritic growth process and form a less fractal morphology (Karma & Rappel, 1998). Therefore, as the phase-field diffusion coefficient drops, the level of branching increases, giving rise to a decrease in the distance between the side branches. The closer side branches can cause a transition from simple pattern morphologies to complex ones, such as needle-like to tree-like dendrites.

Our simulations suggest that tree-like dendrites have a fractal dimension between 1.71 and 1.85, the needle-like pattern is below 1.7, and the seaweed-like one is over 1.85. We will be able to reproduce the dendrites observed in the field by inverting the intrinsic material parameters controlling the pattern-forming process, such as the solute diffusion coefficient. These insights will allow us to decipher the geological environments, such as the supersaturation level. The dendritic pattern may act as a "bar code" equivalent to their internal reaction-diffusion coefficients and the hydrogeological environment that generated these structures. We sought to establish a general criterion for differentiation of the observed field dendrite patterns; thus, we considered the overall qualitative description of the field dendrites and proposed a quantitative measurement of their fractal dimension. In earlier studies, the classification of dendritic growth concentrated on either a qualitative comparison or a fractal dimension calculation. Brener et al. (1996) attempted to divide dendritic morphologies into four groups from shape concerns but their model only considered the effect of supersaturation and anisotropy; as a consequence, only a few observed morphologies in mineral precipitation were generated. Ng and Teh (2009) quantitatively distinguished different manganese dendrites according to different fractal measurements. Nevertheless, their framework yielded similar fractal dimension values for dendrites with noticeably different appearances. Thus, we advance the dendrite pattern characterization by providing a systematic and general criterion that combines both qualitative and quantitative comparisons. Based on numerical and field observations, we have first visually divided mineral dendrites into three categories, namely needle-, tree-, and seaweed-like structures. For dendrites in each category, we then quantitatively distinguish them by measuring their fractal dimension. Our approach ensures that we effectively identify the wide variety of dendrites observed in the field in Section 3.4.1. Although our criterion aims at differentiating mineral dendrites, it extends to a broader set of applications in both living and non-living systems.

We believe that our criterion will assist in the development of computer-aided-vision analysis tools to interpret dendritic patterns from field photographs. Here we have introduced a qualitative classification criterion and provided two morphological diagrams with corresponding quantitative fractal dimensions. We have also tested the possible application to the inversion of the diffusion coefficients and supersaturation level from dendritic morphologies observed on rock surfaces.

Likewise, both Liesegang stripes and dendritic patterns also co-exist in other disciplines, in both living systems, like fungal organisms (Ghanbari et al., 2020), and non-living systems, such as in Li-ion batteries where their growth could spell the end of battery life. Our approach hence provides a generic modelling framework that may also be useful outside the geoscience application and shed light on relevant processes.

5 Conclusion

In this study, we use a phase-field model to systematically investigate the mineral precipitation phenomena, mainly concentrating on dendritic growth. Our simulation results suggest that the transition to Dendritic growth (from Liesegang patterns) is controlled by the magnitude of the diffusion coefficient. Liesegang patterns have a low diffusion coefficient possibly driven by the electrochemical or slow viscous material flow through an intact formation, whereas the dendritic growth shows a high value associated with the subsurface fluid flow along prominent geological discontinuities. We reproduce dendrites observed in the field by first introducing a general criterion to qualitatively and quantitatively classify three dendrite types, namely needle-, tree-, and seaweed-like structures. Our empirical classification scheme, based on visual inspection, was refined by a box-counting method quantifying the fractal geometry. These classification schemes have allowed the construction of phase diagrams for the inversion of key parameters controlling dendritic morphologies. With the inversion of parameters, our simulated patterns match well with the observations in terms of the overall appearance and the fractal di-

mension. Therefore, the presented numerical approach provides a computer-aided-inversion tool capable of analyzing a given pattern or structure from field photographs, which in principle is useful to geological field exploration for resolving the critical reaction-diffusion parameters underpinning the formation mechanism of patterns in nature with potential application to industrial processing.

6 Open Research

The Finite Element Method code and simulation data are available on Mendeley Data (Liu et al., 2023b).

Acknowledgments
The support of the Research Grant Council of Hong Kong (ECS 27203720 and GRF 17206521) and the Australian Research Council (ARC DP200102517, LP170100233) is acknowledged. The funding from the European Union's Horizon 2020 research and innovation programme under the Marie Sklodowska-Curie grant agreement No 777778 (MATHROCKS) is acknowledged.

7 Appendix

Weak form of Phase-field model for mineral precipitation

We solve the coupled nonlinear partial differential equations (16)-(18) using an open-source high-performance phase-field code, PRISMS-PF (DeWitt et al., 2020) based on the finite element library of `deal.II` (Arndt et al., 2020). The library supports adaptive mesh refinement, massively parallel, and matrix-free finite element simulation. We derive the weak formulation to the coupled equations (17) and (18) with the boundary and initial conditions (21)-(23) using the following trial functions

$$\mathcal{S}_i := \{i : \Omega \to \mathbb{R} \mid i \in H^1,\ i = \bar{i} \ \text{ on } \ \Gamma_i\},\ i \in \{c, \phi, \mu\} \tag{26}$$

and test functions as

$$\mathcal{V}_i := \{j : \Omega \to \mathbb{R} \mid j \in H^1,\ j = 0 \ \text{ on } \ \Gamma_i\},\ j \in \{\psi, \eta, \omega\} \tag{27}$$

and integration by parts. We use the forward Euler method for time marching; thus, the corresponding weak forms become

$$\int_\Omega \eta\phi^{n+1}\, dV = \int_\Omega \eta \underbrace{\left(\phi^n + \frac{\Delta t \mu^n}{\tau(\boldsymbol{n})}\right)}_{r_\phi} dV \tag{28}$$

$$\begin{aligned}\int_\Omega \omega\mu^{n+1}\, dV = \int_\Omega \omega \underbrace{\left[\phi^n - \lambda u\left(1 - (\phi^n)^2\right)\right]\left(1 - (\phi^n)^2\right)}_{r_\mu} \\ + \nabla\omega \cdot \underbrace{\Bigg[- \left(W^2 \frac{\partial \phi^n}{\partial x} + W_0 \epsilon_m m W(\theta^n) \sin\left[m\left(\theta^n - \theta_0\right)\right] \frac{\partial \phi^n}{\partial y}\right)\hat{x}}_{r_{\phi x}} \\ \underbrace{- \left(W^2 \frac{\partial \phi^n}{\partial y} - W_0 \epsilon_m m W(\theta^n) \sin\left[m\left(\theta^n - \theta_0\right)\right] \frac{\partial \phi^n}{\partial x}\right)\hat{y}\Bigg]}_{r_{\phi x}}\, dV\end{aligned} \tag{29}$$

$$\int_\Omega \psi c^{n+1}\, dV = \int_\Omega \psi \underbrace{\left(c^n + \frac{A\mu^n \Delta t}{\tau(\boldsymbol{n})}\right)}_{r_c} + \nabla\psi \cdot \underbrace{(-D\Delta t \nabla c^n)}_{r_{cx}}\, dV + \int_\Gamma \psi(\Delta t D) j_\phi^n\, dS \tag{30}$$

The numerical results solve (28)-(30) using PRISMS-PF, which allows for future extension of this study to a 3D scenario with its adaptive mesh refinement feature.

References

Antal, T., Droz, M., Magnin, J., & Rácz, Z. (1999). Formation of Liesegang patterns: A spinodal decomposition scenario. *Physical Review Letters*, *83*(15), 2880.

Antal, T., Droz, M., Magnin, J., Rácz, Z., & Zrinyi, M. (1998). Derivation of the Matalon-Packter law for Liesegang patterns. *The Journal of Chemical Physics*, *109*(21), 9479–9486.

Arguello, M. E., Labanda, N. A., Calo, V. M., Gumulya, M., Utikar, R., & Derksen, J. (2022). Dendrite formation in rechargeable lithium-metal batteries: Phase-field modeling using open-source finite element library. *Journal of Energy Storage*, *53*, 104892.

Arndt, D., Bangerth, W., Blais, B., Clevenger, T. C., Fehling, M., Grayver, A. V., ... Wells, D. (2020). The `deal.II` Library, Version 9.2. *Journal of Numerical Mathematics*, *28*(3), 131-146.

Bayirli, M., Ozbey, T., & Gulgonul, I. (2018). Determination of Poly Morphological Transitions of Dendrites on Natural Magnesite Surfaces. *International Journal of Scientific and Technological Research*, *4*(4), 109–116.

Behnoudfar, P., Hobbs, B. E., Ord, A., Espath, L., & Calo, V. M. (2022). Localized folding of thick layers. *Journal of Structural Geology*, *161*, 104669.

Bhagat, K., & Rudraraju, S. (2022). Modeling of dendritic solidification and numerical analysis of the phase-field approach to model complex morphologies in alloys. *Engineering with Computers*, 1–19.

Brener, E., Müller-Krumbhaar, H., & Temkin, D. (1996). Structure formation and the morphology diagram of possible structures in two-dimensional diffusional growth. *Physical Review E*, *54*(3), 2714.

Büki, A., Kárpáti-Smidróczki, É., & Zrínyi, M. (1995). Computer simulation of regular Liesegang structures. *The Journal of Chemical Physics*, *103*(23), 10387–10392.

Caginalp, G. (1986). An analysis of a phase field model of a free boundary. *Archive for Rational Mechanics and Analysis*, *92*, 205–245.

Caginalp, G. (1989). Stefan and Hele-Shaw type models as asymptotic limits of the phase-field equations. *Physical Review A*, *39*(11), 5887.

Chopard, B., Herrmann, H., & Vicsek, T. (1991). Structure and growth mechanism of mineral dendrites. *Nature*, *353*(6343), 409–412.

Chopard, B., Luthi, P., & Droz, M. (1994). Reaction-diffusion cellular automata model for the formation of Leisegang patterns. *Physical Review Letters*, *72*(9), 1384.

Cier, R., Rojas, S., & Calo, V. (2021). Automatically adaptive, stabilized FEM via residual minimization for heterogeneous, anisotropic advection–diffusion–reaction problems. *Computer Methods in Applied Mechanics and Engineering*, *385*, 114027.

Collins, J. B., & Levine, H. (1985). Diffuse interface model of diffusion-limited crystal growth. *Physical Review B*, *31*(9), 6119.

DeWitt, S., Rudraraju, S., Montiel, D., Andrews, W. B., & Thornton, K. (2020). PRISMS-PF: A general framework for phase-field modeling with a matrix-free finite element method. *npj Computational Materials*, *6*(1), 1–12.

Espath, L. (2021). On the control volume arbitrariness in the Navier–Stokes equation. *Physics of Fluids*, *33*, 015110.

Espath, L., & Calo, V. (2021). Phase-field gradient theory. *Zeitschrift fur Angewandte Mathematik und Physik*, *72*.

Fei, F., Choo, J., Liu, C., & White, J. A. (2022). Phase-field modeling of rock fractures with roughness. *International Journal for Numerical and Analytical Methods in Geomechanics*, *46*(5), 841–868.

Furui, K., Abe, T., Watanabe, T., & Yoshioka, K. (2022). Phase-field modeling of wormhole formation and growth in carbonate matrix acidizing. *Journal of*

Petroleum Science and Engineering, *209*, 109866.

García-Ruiz, J. M., & Otálora, F. (2015). Crystal growth in geology: patterns on the rocks. In *Handbook of crystal growth* (pp. 1–43).

García-Ruiz, J. M., Otálora, F., Sanchez-Navas, A., & Higes-Rolando, F. J. (1994). The formation of manganese dendrites as the mineral record of flow structures. *Fractals and Dynamic Systems in Geoscience*, 307–318.

Ghanbari, F., Costanzo, F., Hughes, D., & Peco, C. (2020). Phase-field modeling of constrained interactive fungal networks. *Journal of the Mechanics and Physics of Solids*, *145*, 104160.

Giraldo, J., & Calo, V. (2023). An adaptive in space, stabilized finite element method via residual minimization for linear and nonlinear unsteady advection-diffusion-reaction equations. *Mathematical and Computational Applications*, *28*(1).

Gómez, H., Calo, V. M., Bazilevs, Y., & Hughes, T. J. (2008). Isogeometric analysis of the Cahn–Hilliard phase-field model. *Computer Methods in Applied Mechanics and Engineering*, *197*(49-50), 4333–4352.

Hawkins, C., Angheluta, L., & Jamtveit, B. (2014). Hydrodynamic shadowing effect during precipitation of dendrites in channel flow. *Physical Review E*, *89*(2), 022402.

Hu, X., Li, R., & Tang, T. (2009). A multi-mesh adaptive finite element approximation to phase field models. *Communications in Computational Physics*, *5*(5), 1012–1029.

Ivantsov, G. (1947). The temperature field around a spherical, cylindrical, or pointed crystal growing in a cooling solution. In *Dokl. Akad. Nauk SSSR* (Vol. 58, pp. 567–569).

Kang, Q., Zhang, D., & Chen, S. (2003). Simulation of dissolution and precipitation in porous media. *Journal of Geophysical Research: Solid Earth*, *108*(B10).

Karma, A., & Rappel, W.-J. (1998). Quantitative phase-field modeling of dendritic growth in two and three dimensions. *Physical Review E*, *57*(4), 4323.

Karma, A., & Rappel, W.-J. (1999). Phase-field model of dendritic sidebranching with thermal noise. *Physical Review E*, *60*(4), 3614.

Kobayashi, R. (1993). Modeling and numerical simulations of dendritic crystal growth. *Physica D: Nonlinear Phenomena*, *63*(3-4), 410–423.

Kundin, J., & Steinbach, I. (2019). Comparative study of different anisotropy and potential formulations of phase-field models for dendritic solidification. *Computational Materials Science*, *170*, 109197.

Ladd, A. J., & Szymczak, P. (2021). Reactive flows in porous media: challenges in theoretical and numerical methods. *Annual review of chemical and biomolecular engineering*, *12*, 543–571.

Langer, J. S. (1980). Instabilities and pattern formation in crystal growth. *Reviews of Modern Physics*, *52*(1), 1.

Langer, J. S. (1989). Dendrites, viscous fingers, and the theory of pattern formation. *Science*, *243*(4895), 1150–1156.

Li, X., Huang, H., & Meakin, P. (2008). Level set simulation of coupled advection-diffusion and pore structure evolution due to mineral precipitation in porous media. *Water Resources Research*, *44*(12).

Liesegang, R. E. (1906). Eine scheinbar chemische Fernwirkung. *Annalen der Physik*, *324*(2), 395-406.

Lin, C., Liu, K., Ruan, H., & Wang, B. (2022). Mechano-electrochemical phase field modeling for formation and modulation of dendritic pattern: Application to uranium recovery from spent nuclear fuel. *Materials & Design*, *213*, 110322.

Liu, C., Calo, V., Regenauer-Lieb, K., & Hu, M. (2023a). Coefficients of reaction-diffusion processes derived from patterns in rocks. *Journal of Geophysical Research: Solid Earth*, *128*(5), e2022JB026253.

Liu, C., Calo, V., Regenauer-Lieb, K., & Hu, M. (2023b). *Dendritic growth and*

Liesegang patterns: Inverting the driving and triggering mechanisms [Dataset]. Mendeley Data. Retrieved from `https://data.mendeley.com/v1/datasets/vzp55nbbj9/draft?preview=1` doi: 10.17632/vzp55nbbj9.2

Liu, C., Hu, M., & Regenauer-Lieb, K. (2022). Liesegang Patterns Interpreted as a Chemo-Hydromechanical Instability. In *Multiscale Processes of Instability, Deformation and Fracturing in Geomaterials: Proceedings of 12th International Workshop on Bifurcation and Degradation in Geomechanics* (pp. 59–66).

Måløy, K. J., Feder, J., & Jøssang, T. (1985). Viscous fingering fractals in porous media. *Physical Review Letters*, *55*(24), 2688.

Mandelbrot, B. B. (1982). *The Fractal Geometry of Nature* (Vol. 1). W. H. freeman New York.

Matalon, R., & Packter, A. (1955). The Liesegang phenomenon. I. Sol protection and diffusion. *Journal of Colloid Science*, *10*(1), 46–62.

Merdan, Z., & Bayirli, M. (2005). Computation of the fractal pattern in manganese dendrites. *Chinese Physics Letters*, *22*(8), 2112.

Moisy, F. (2008). *boxcount* [Software]. MATLAB Central File Exchange. Retrieved from `https://www.mathworks.com/matlabcentral/fileexchange/13063-boxcount` (accessed on 30-1-2023)

Molins, S., Soulaine, C., Prasianakis, N. I., Abbasi, A., Poncet, P., Ladd, A. J., ... others (2021). Simulation of mineral dissolution at the pore scale with evolving fluid-solid interfaces: Review of approaches and benchmark problem set. *Computational Geosciences*, *25*, 1285–1318.

Mullins, W. W., & Sekerka, R. F. (1963). Morphological stability of a particle growing by diffusion or heat flow. *Journal of Applied Physics*, *34*(2), 323–329.

Ng, T., & Teh, G. (2009). Fractal and shape analyses of manganese dendrites on vein quartz. *Bulletin of the Geological Society of Malaysia*, *55*, 73–79.

Ostwald, W. (1902). *Lehrbuch der allgemeinen Chemie* (Vol. 2). W. Engelmann.

Peco, C., Liu, Y., Rhea, C., & Dolbow, J. (2019). Models and simulations of surfactant-driven fracture in particle rafts. *International Journal of Solids and Structures*, *156*, 194–209.

Rosam, J., Jimack, P. K., & Mullis, A. (2007). A fully implicit, fully adaptive time and space discretisation method for phase-field simulation of binary alloy solidification. *Journal of Computational Physics*, *225*(2), 1271–1287.

Singer, H., Singer-Loginova, I., Bilgram, J., & Amberg, G. (2006). Morphology diagram of thermal dendritic solidification by means of phase-field models in two and three dimensions. *Journal of Crystal Growth*, *296*(1), 58–68.

Soulaine, C., & Tchelepi, H. A. (2016). Micro-continuum approach for pore-scale simulation of subsurface processes. *Transport in porous media*, *113*, 431–456.

Steefel, C. I., & Lasaga, A. C. (1994). A coupled model for transport of multiple chemical species and kinetic precipitation/dissolution reactions with application to reactive flow in single phase hydrothermal systems. *American Journal of science*, *294*(5), 529–592.

Steefel, C. I., & Maher, K. (2009). Fluid-rock interaction: A reactive transport approach. *Reviews in mineralogy and geochemistry*, *70*(1), 485–532.

Swartzlow, C. R. (1934). Two dimensional dendrites and their origin. *American Mineralogist*, *19*(9), 403–411.

Tartakovsky, A. M., Meakin, P., Scheibe, T. D., & West, R. M. E. (2007). Simulations of reactive transport and precipitation with smoothed particle hydrodynamics. *Journal of Computational Physics*, *222*(2), 654–672.

Thomas, S., Lagzi, I., Molnár Jr, F., & Rácz, Z. (2013). Probability of the Emergence of Helical Precipitation Patterns in the Wake of Reaction-Diffusion Fronts. *Physical Review Letters*, *110*(7), 078303.

Vicsek, T. (1992). *Fractal Growth Phenomena*. World scientific.

Vignal, P., Collier, N., Dalcin, L., Brown, D., & Calo, V. (2017). An energy-stable time-integrator for phase-field models. *Computer Methods in Applied Mechan-*

ics and Engineering, *316*, 1179-1214.

Wang, Y., Chan, M. A., & Merino, E. (2015). Self-organized iron-oxide cementation geometry as an indicator of paleo-flows. *Scientific Reports*, *5*(1), 1–15.

Witten, T. A., & Sander, L. M. (1983). Diffusion-limited aggregation. *Physical Review B*, *27*(9), 5686.

Xu, T., Apps, J. A., & Pruess, K. (2003). Reactive geochemical transport simulation to study mineral trapping for co2 disposal in deep arenaceous formations. *Journal of Geophysical Research: Solid Earth*, *108*(B2).

Xu, Z., & Meakin, P. (2008). Phase-field modeling of solute precipitation and dissolution. *The Journal of Chemical Physics*, *129*(1), 014705.

Xu, Z., & Meakin, P. (2011). Phase-field modeling of two-dimensional solute precipitation/dissolution: Solid fingers and diffusion-limited precipitation. *The Journal of Chemical Physics*, *134*(4), 044137.

Yamaguchi, T., Kuhnert, L., Nagy-Ungvarai, Z., Müller, S., & Hess, B. (1991). Gel systems for the belousov-zhabotinskii reaction. *The Journal of Physical Chemistry*, *95*(15), 5831–5837.